

Variation of the subsidence parameters, effective thermal conductivity, and mantle dynamics

Supplementary Material

Adam C., S. D. King, V. Vidal, M. Rabinowicz, A. Jalobeanu, and M. Yoshida

1. Fit of the bathymetry trend - The outliers method

Here we explain in more details how we quantitatively assess the linear relationship between the seafloor depth and the square-root of age, along the considered age trajectories. The main problem is that bathymetry profiles display many geologic features such as seamounts, hotspot swells, fracture zones, etc., which should not be taken into account in this linear regression. Rather than removing manually the corresponding zones, as was done previously in the literature, we chose to develop a method which makes it possible to capture the general bathymetric trend with a simple linear regression, without the bias introduced by the presence of outliers. In our problem, the amount of outliers is significant and we need to use a robust estimation method. Robust estimation has been available for almost 50 years (Huber, 1964), and robust regression in the presence of outliers has been addressed in various ways (Rousseuw and Leroy, 1987), however none of these methods is both unsupervised and designed to handle positive outliers, as in our data. First, most common robust estimation approaches rely on a non-quadratic energy function, which does not penalize large errors as much as small ones, thus providing more robust results than least squares approaches, which are based on quadratic penalty functions. Usually the function is chosen arbitrarily and user interaction is therefore required. Equivalently, in a probabilistic approach to robust estimation, the noise distribution is designed to have a heavier tail than a Gaussian, thus accounting for outliers - for instance by using a mixture of Gaussian and uniform distribution, or a Laplacian. The mixture or the distribution are chosen manually, which we want to avoid. Moreover, few methods allow for asymmetric outliers; usually the energy function (or

noise distribution) is symmetric, and negative outliers are allowed, which is not appropriate for our data. A few approaches using asymmetric functions can be found, but they are rare, see for instance Takeuchi et al. (2002), where quantiles are used to handle the outlier distribution, which yields a rather complex implementation.

We define a simpler, automatic method that handles positive outliers, using probabilistic modeling and Bayesian inference. Recently, fully automated robust regression solutions have been proposed in the computer vision community (Fransens et al., 2006). Such solutions achieve automation by using an explicit modeling of outliers (as opposed to implicit, where a function or a probability density is chosen manually), defining a set of indicator variables or labels, and estimating all the related parameters within a Bayesian framework. In addition to the quantities of interest, there are extra parameters that define the outlier distribution, the outlier rate and the inlier noise variance. We modify this approach by imposing a positivity constraint on the outliers, by using a uniform distribution between 0 and M where $M > 0$ is the upper bound. As an added value, we compute the uncertainties on the parameters of interest.

We also use an Expectation-Maximization algorithm (EM) (Dempster et al., 1977) to estimate the parameters. This algorithm is similar to a reweighted least squares estimation technique, however the weights are actual probabilities, and the whole approach amounts to minimizing an energy constructed using a probabilistic model.

In the following, y_i and x_i denote the measurement and the predictor variables, respectively (in our case, the bathymetry and the square root of the seafloor age). The slope and intercept are denoted by A and B . Let us define the residuals $r_i = y_i - Ax_i - B$. We define the labels s_i , equal to 0 for inliers and 1 for outliers. Then, we define the inlier and outlier conditional probability distributions as G_i and U_i (implicitly conditioned upon the current parameter values, omitted for the sake of clarity):

$$G_i \equiv p(y_i | x_i, s_i = 0) = \frac{1}{\sigma \sqrt{2\pi}} e^{-r_i^2 / 2\sigma^2} \quad (\text{S1})$$

$$U_i \equiv p(y_i | x_i, s_i=1) = \frac{1}{M} \mathbf{1}_{0 \leq r_i \leq M} \quad (\text{S2})$$

where σ^2 is the inlier noise variance, and M the outlier upper bound. To complete the model we need to define the prior inlier rate uniformly as $p(s_i=0)=\lambda$.

We use the EM algorithm to estimate A and B , σ^2 , but also M and λ automatically; this algorithm was designed to handle incomplete data, in this case the unknown set of labels s_i . We start by setting $\lambda = 0.5$ and $M = M_0$ (approximate outlier range). We run a classical non-robust regression to get initial values of A , B and σ^2 . Then we alternate the E and M steps.

The E step consists of computing π_i , the posterior probability of the label given the data $p(s_i=0 | y_i, x_i)$ and the current parameter values.

$$\hat{\pi}_i = \frac{\lambda G_i}{\lambda G_i + (1 - \lambda) U_i} \quad (\text{S3})$$

The M step consists of updating the parameters of interest through a weighted regression by using π_i as weights. We do not give here the explicit formulas. They can be easily obtained by replacing all the sums of the simple regression case (Weisstein) by weighted sums, and the number of data points by $\sum_i \pi_i$. Let n denote the number of data points; the inlier rate λ and upper bound M are updated by:

$$\hat{\lambda} = \frac{\sum_i \pi_i}{n} \quad \text{and} \quad \hat{M} = 2 \frac{\sum_i (1 - \pi_i) r_i}{\sum_i (1 - \pi_i)} \quad (\text{S4})$$

The algorithm requires only a few dozen iterations to converge; fewer outliers means faster convergence. At the end, we obtain optimal values of the parameters of interest that are robust to outliers, and also the values of the two extra parameters required by the explicit outlier model. Moreover, we also compute standard errors on A and B , again replacing the existing formulas by their weighted counterparts.

In Fig. S1 we display the fit of the bathymetry versus the square root of the age of the seafloor through the outliers method for the major oceans.

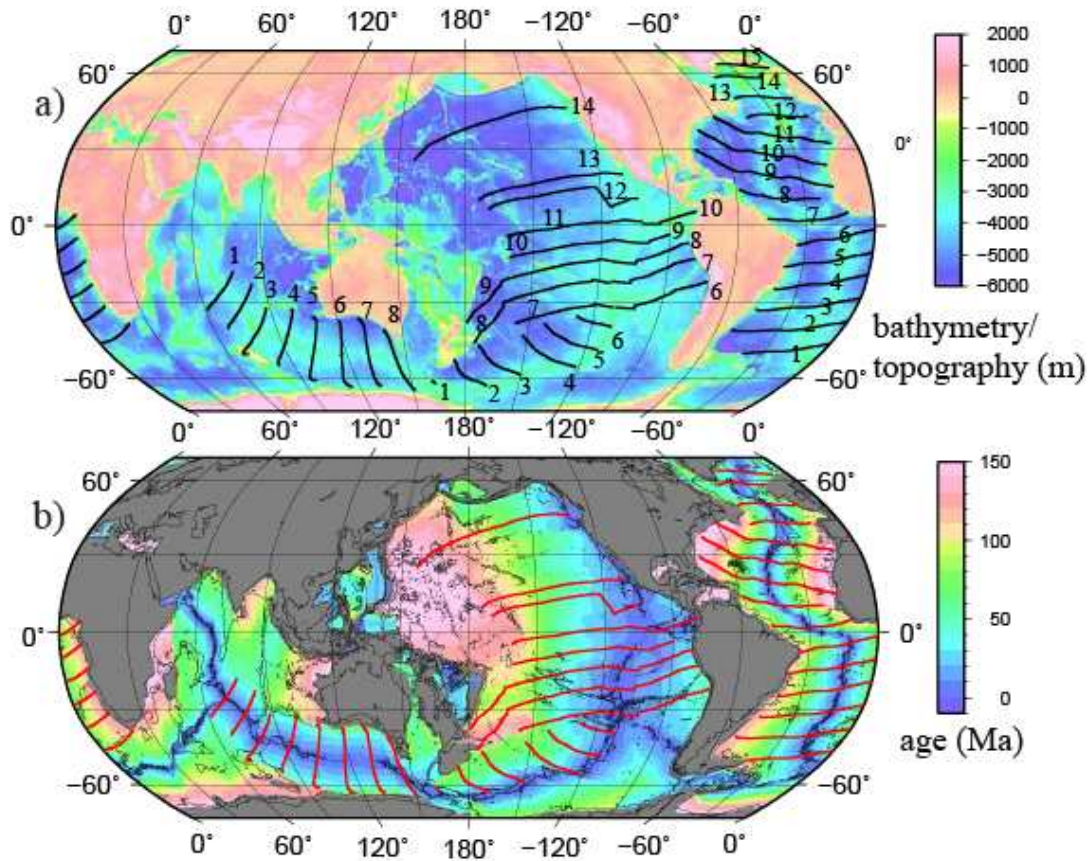


Figure S1: Fit of the bathymetry versus the square root of the age of the lithosphere through the outliers method. Emplacement of the age trajectories on the bathymetry (a) and seafloor age maps (b). (c-g) Fit of the bathymetry versus the square root of the age of the lithosphere for the major oceanic plates. c) the Pacific plate, d) Nazca plate, e) West Atlantic, f) East Atlantic, g) Indian plate. The arrow at the end of the profiles is the departure point defined as the location from where the bathymetry departs from the linear trend versus the square root of the seafloor age and never recovers it. We report the age of the departure from the linear trend in Ma above the arrow.

c) Pacific plate

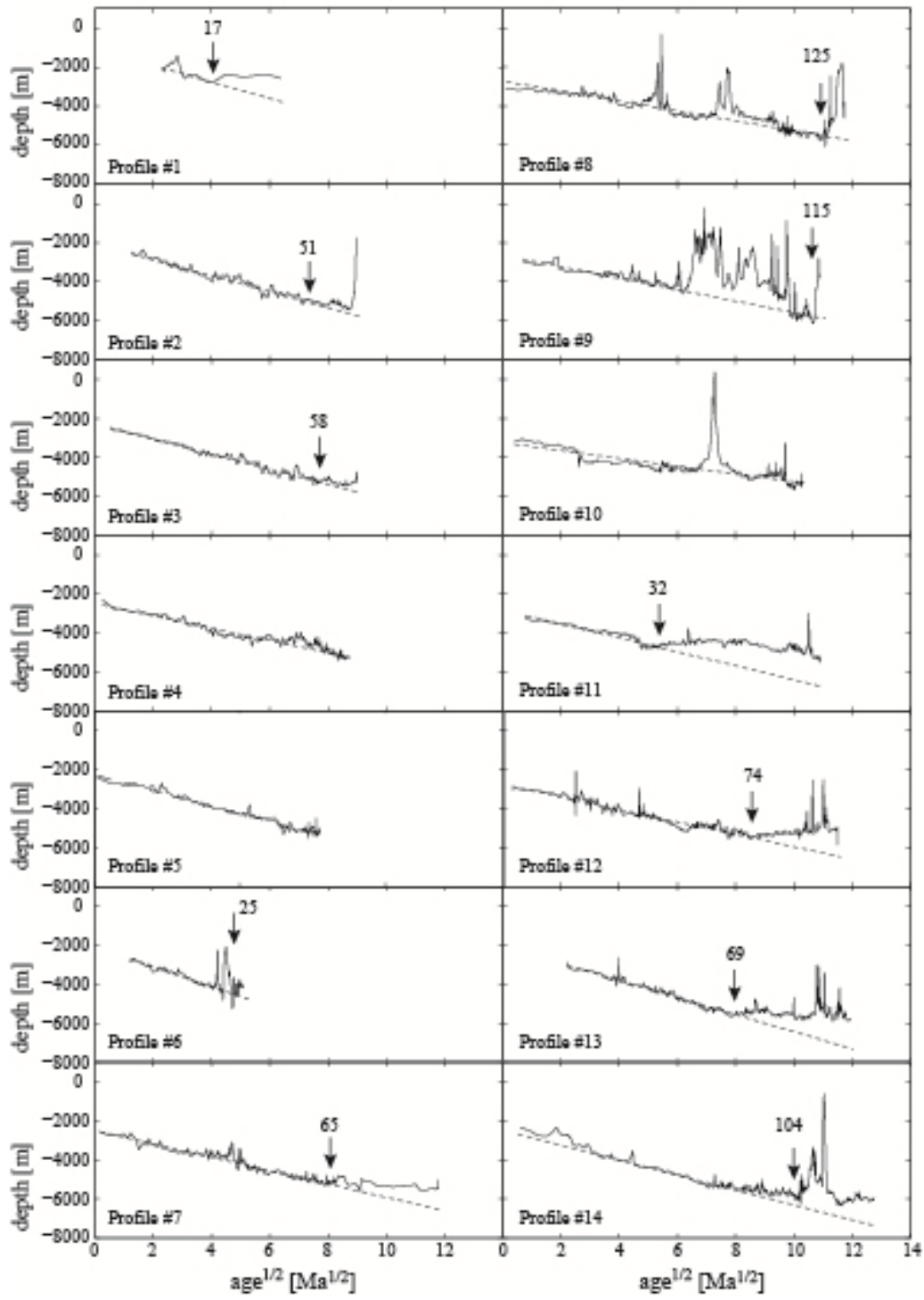


Figure S1 (continued)

d) Nazca plate

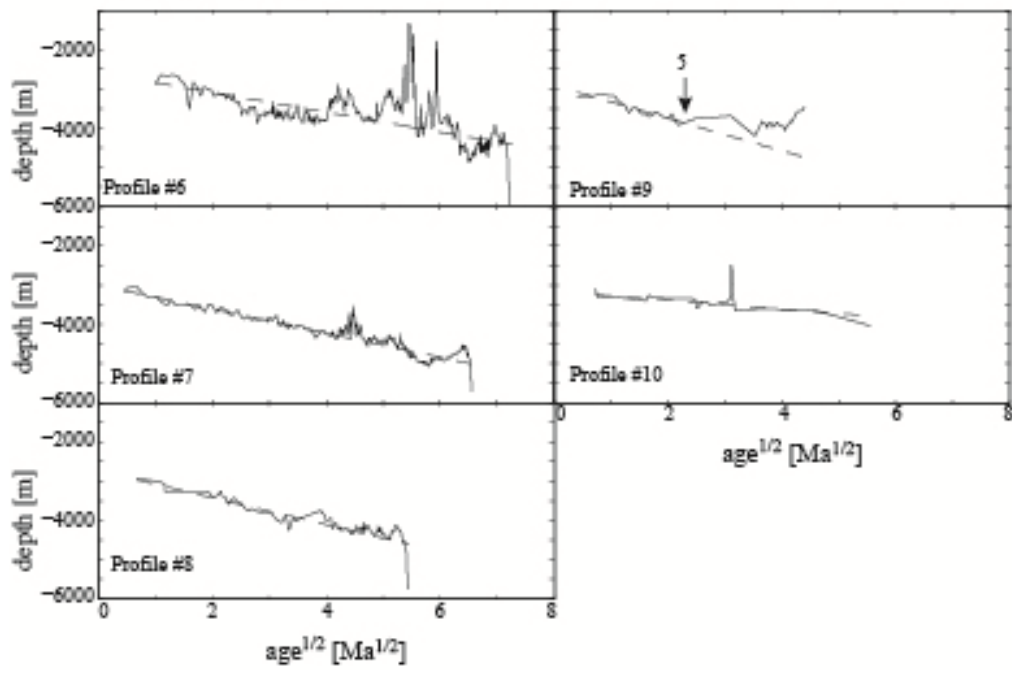


Figure S1 (continued)

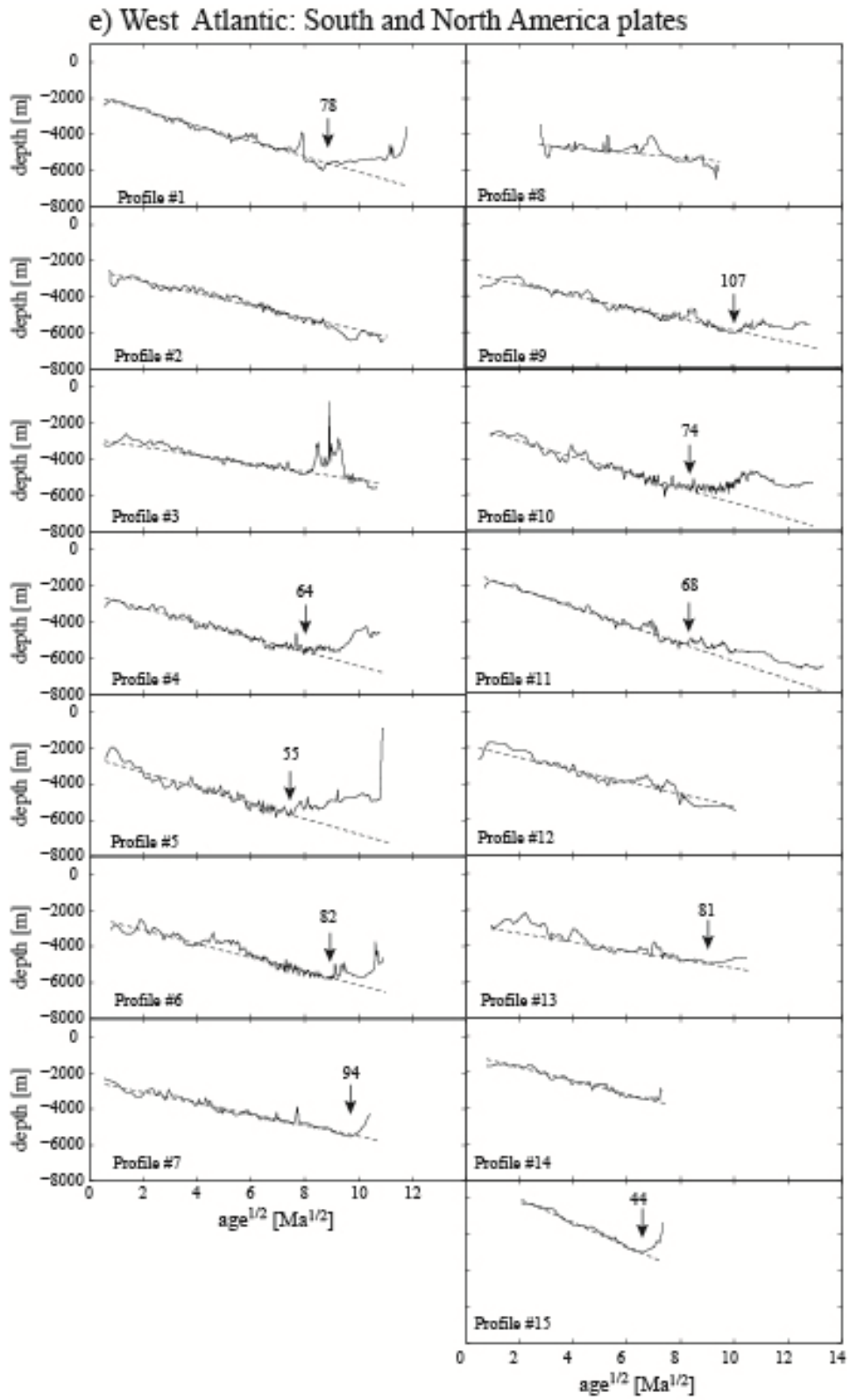


Figure S1 (continued)

f) East Atlantic: Eurasia and Nubia plates

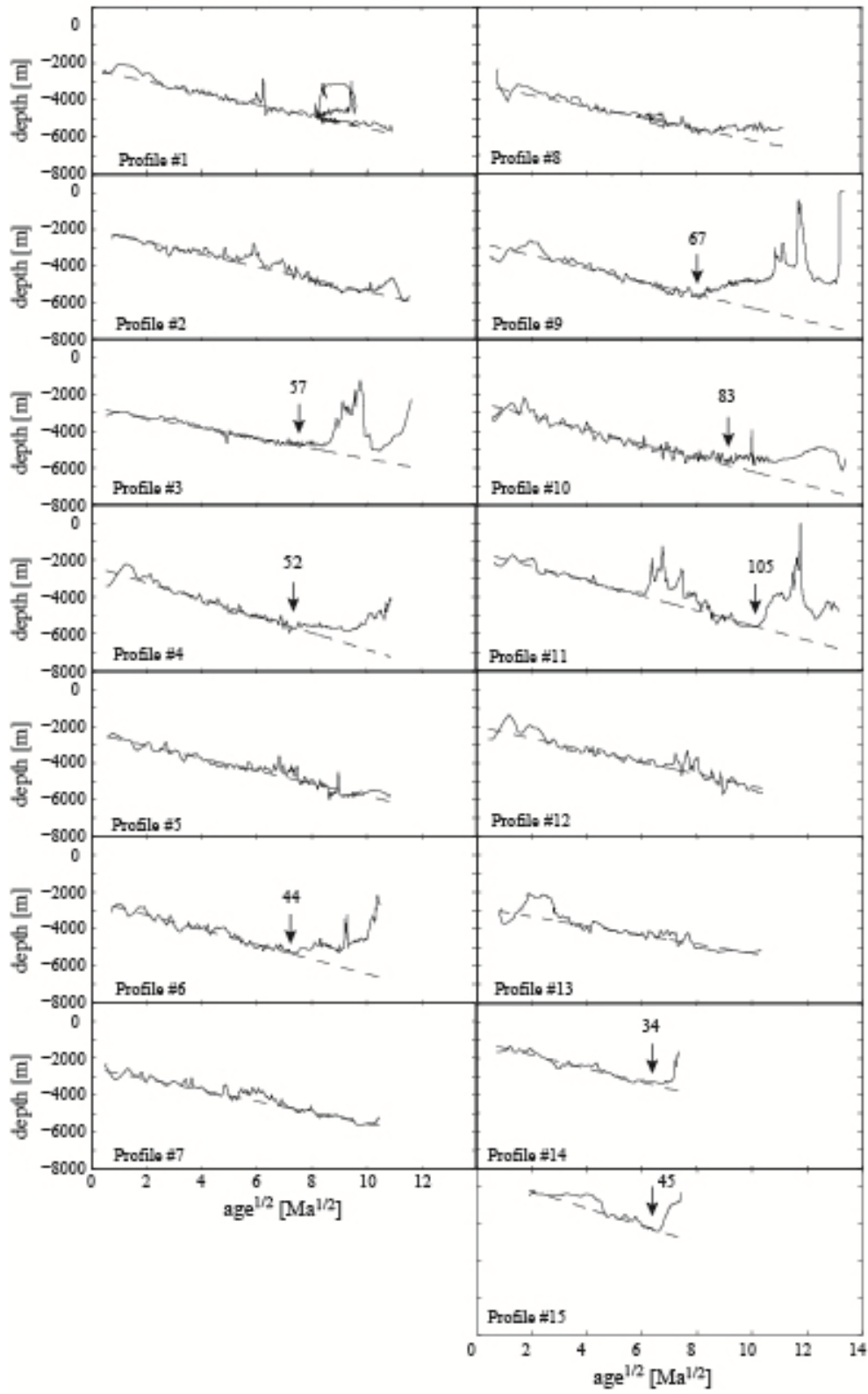


Figure S1 (continued)

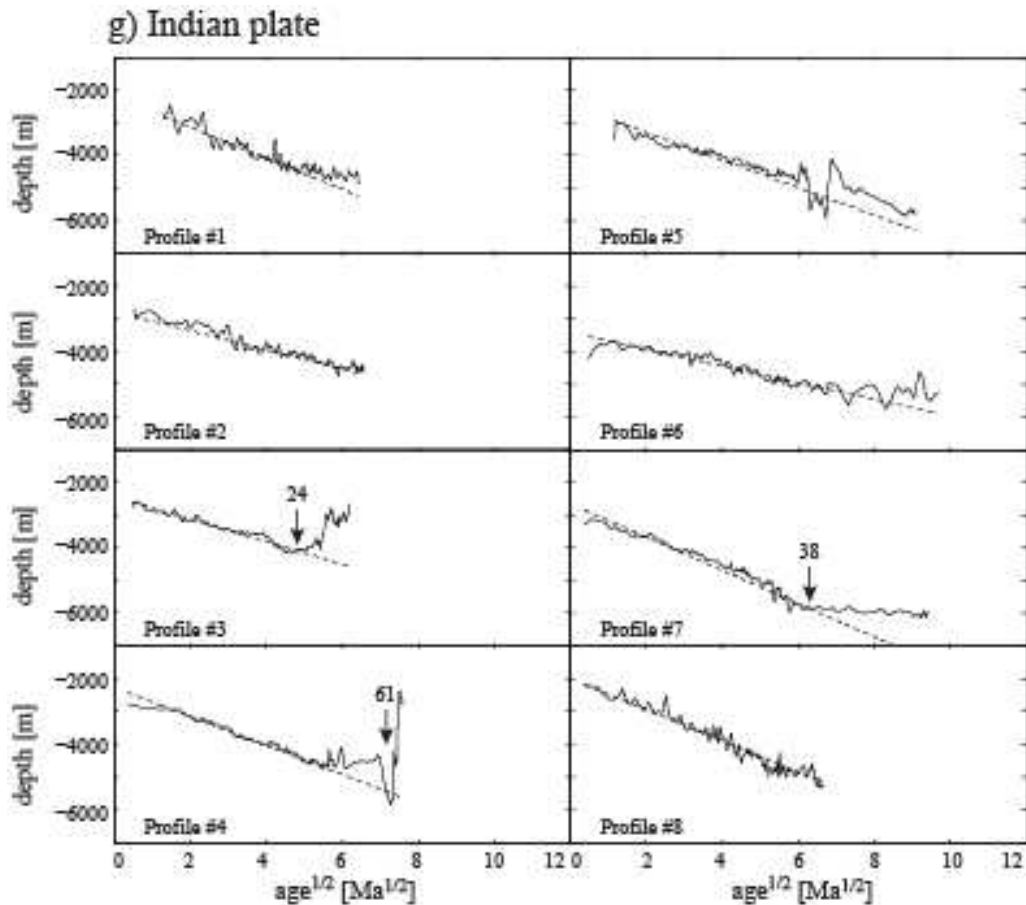


Figure S1 (continued)

2 Fit of the bathymetry trend - the MiFil method

The MiFil method (for Minimization and Filtering) is a filtering method especially designed for the characterization of depth anomalies (Adam et al., 2005). It requires two stages: the first is to approximately remove the island/volcanic component of topography by minimizing the depth anomaly. During the second stage the minimized grid is filtered through a median filter in order to smooth the shape and totally remove the remaining small spatial length scale topography.

One of the main problems with the MiFil method is that the median filter used during the second stage is sensitive to slopes. Therefore we have to remove the subsidence trend before filtering. Since this subsidence trend is what we are ultimately looking for in the

present study, this could appear quite problematic. However, it is only necessary to approximately remove this trend. Several tests have been performed with different subsidence trends. We have removed 1) the subsidence model proposed by Parsons and Sclater (1977), 2) the subsidence model proposed by Stein and Stein (1992), 3) and several half space models we designed, where the seafloor depth, z , is approximated by $z = a\sqrt{\text{age}} + b$, where a and b are constants we vary. In particular we vary a between 250 and 400 m Myr^{-1/2}. Note that $a=365$ m Myr^{-1/2} for Stein and Stein (1992), and $a= 350$ m Myr^{-1/2} for Parsons and Sclater (1977). Once the depth anomaly is obtained, it is filtered with MiFil. We then add the subsidence trend we first removed, and perform a linear regression between the filtered bathymetry and the square root of the seafloor age. We derive the subsidence rate, τ , and the seafloor's depth at the ridge, Z_R , fitted from our regression.

Fig. S2 illustrates the influence of the considered subsidence model. In panel a), we report in black the bathymetry along the profile represented in the inset, in blue the bathymetry filtered considering Stein and Stein's (1992) subsidence model, and in red, the bathymetry filtered considering Parsons and Sclater's (1977) subsidence model. The radius of the minimizing filter is $r=50$ km, the radius of the median filter is $R=700$ km, based on previous results (Adam and Bonneville, 2005). In panel b), we report the theoretical depth obtained through our fit by considering either Parsons and Sclater (1977) or Stein and Stein (1992) subsidence model.. There are no noticeable differences between this fits. To have a more global view of the influence of this parameter, we report the subsidence rate (in panel c) and ridge depth (in panel d) found through the linear regression between the filtered bathymetry and the square root of age over the Pacific plate. There again, no noticeable difference are introduced by the choice of the initial subsidence model. Since no noticeable difference is introduced by the choice of the subsidence model, in the following we will present only the results found with Stein and Stein's (1992) subsidence model.

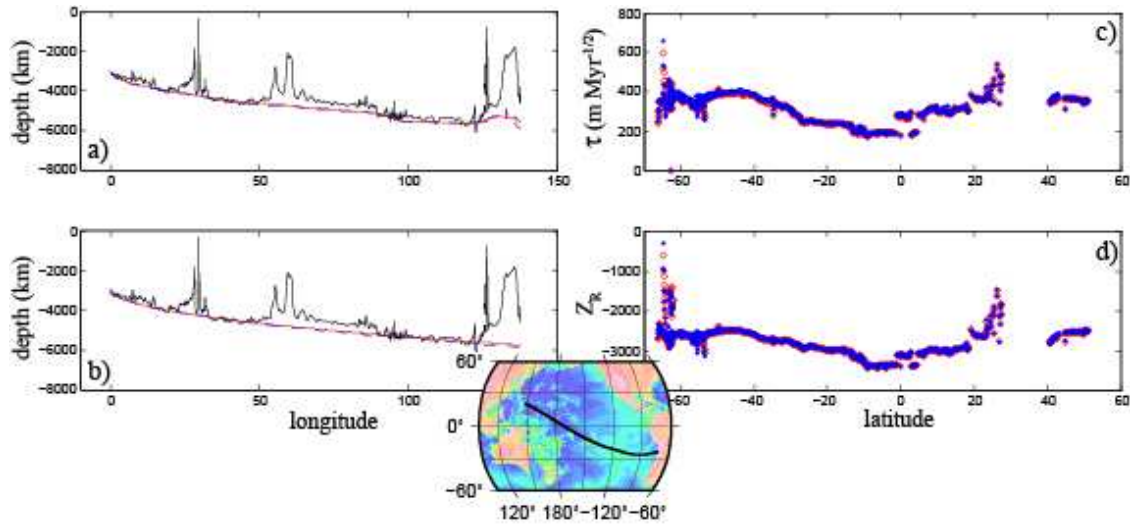


Figure S2: Influence of the initial subsidence model on the determination of the subsidence trend with the MiFil method. a) Bathymetry (black line) and filtered bathymetry considering either Stein and Stein's (1992) subsidence model (in blue), or filtered considering Parsons and Sclater's (1977) subsidence model (in red). b) Bathymetry (black line) and theoretical depth provided by our fit considering either Stein and Stein's (1992) subsidence model (in blue), or Parsons and Sclater's (1977) subsidence model (in red). c) and d) Subsidence rate (c) and ridge height (d) found through our fit considering the previous initial subsidence models, as a function of the ridge latitude. The color code is the same than in the previous panels [$r=50$ km, $R=700$ km].

Another issue with the MiFil method is that the final result may be sensitive to the model parameters, i.e. the radii of the minimizing and median filters (hereafter r and R respectively). These parameters are chosen by considering the spatial length scale of the features to remove. To test the influence of these parameters we vary them in a realistic range ($r=25-75$ km, $R=500-800$ km). In fig. S3, we report the variations induced by varying the filtering parameters. Adam and Bonneville (2005) show that the volcanoes and swells associated with hotspot chains are completely removed for the radii $r=50$ km and $R=700$ km. We will consider this as the standard filter, and represent it in red in the Fig. S3. We also test a filter with smaller radii ($r=25$ km and $R=500$ km), reported in green, and bigger radii ($r=75$ km and $R=800$ km), in blue in Fig. S3.

In panel a), we report in black the bathymetry and the bathymetry filtered through these filters along the profile represented in the inset of fig. S2. In panel b), we report the theoretical depth obtained by our fit. To have a more global view of the influence of the filter radii, we report the subsidence rate (in panel c) and ridge depth (in panel d) found through our fit over the Pacific plate, for different filtering parameters. There again, no noticeable difference are introduced by varying the filter radii in a reasonable range. In the following, the fits obtained with MiFil are with $r=50$ km and $R=700$ km.

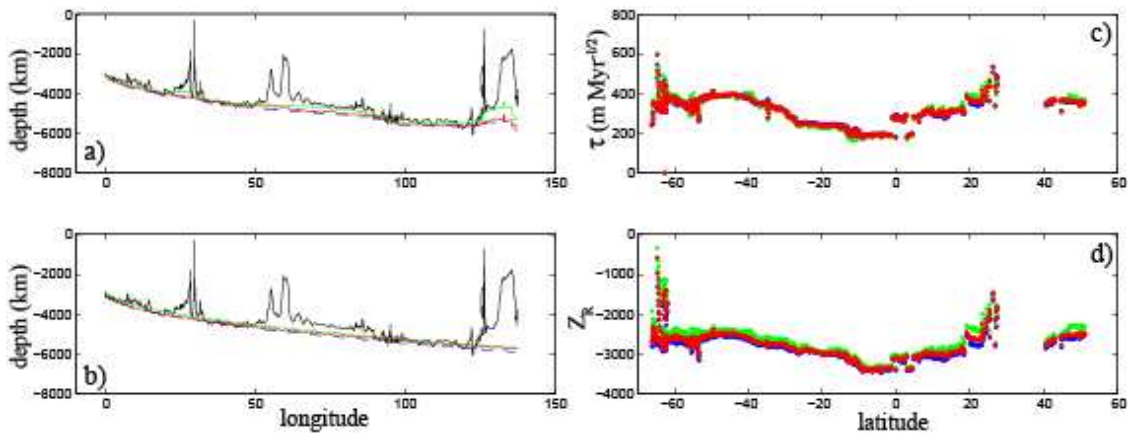


Figure S3: Influence of the filtering parameters for the Pacific plate. The bathymetry is reported in black in panels a) and b), along the profile represented on the inset of Fig. S2. The color code represents the different filtering parameters: green $r=25$ km and $R=500$ km, red $r=50$ km and $R=700$ km, blue $r=75$ km and $R=800$ km. a) Filtered bathymetry; b) Depth obtained with our fit; c) Subsidence rate and d) ridge height found through our fit considering the different filtering parameters.

In Figure S4 we report, along the same profile, the main seafloor trend provided by the outliers method (in blue) and by the MiFil method (in red). Although these fits are slightly different, it is hard to say which one represents the best approximation of the subsidence trend. The scope here is not to choose a particular one, but to provide trends through two completely independent methods, in order to make sure that the variation of the obtained subsidence parameters is not an artifact of the method. Both methods have pro and cons. With the outliers method, the fit is obtained automatically. The only parameter is the outlier range, M_0 , which we fix at 1000 m, the range of the geological

features representing the outliers. There are no noticeable alterations of the final fit if this parameter varies in the range of 500 to 5000 m. With MiFil, the filtering parameters have to be chosen. However, we demonstrate that varying these parameters within a realistic range does not noticeably affect the final results. Moreover, MiFil filters a 2D grid and then provides a smoother variation of the subsidence parameters.

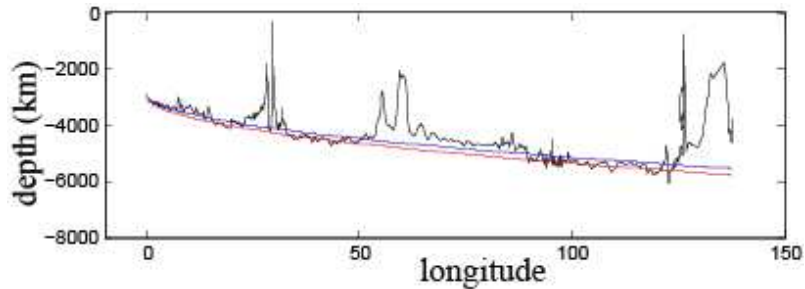


Figure S4: Fit of the subsidence trend along the profile reported on the inset of Fig. S2. The black line is the bathymetry, the blue and red curves are the main seafloor trends provided by the outliers and MiFil method, respectively.

3. Mantle dynamics modeling

In the second part of this study, we investigate the mantle dynamics. We perform a series of numerical simulations of instantaneous mantle flow in a global three-dimensional (3D) spherical-shell geometry, based on the “S40RTS” (Ritsema et al., 2010). We convert the seismic velocities anomalies into density anomalies and model the instantaneous flow they induce. In the following, we describe the numerical model and its parameters, as well as the method we use to obtain the dynamic topography.

3.1 Basic equations and methods

To solve for instantaneous mantle flow driven by density anomalies in a global 3D spherical shell geometry using spherical polar coordinates (r, θ, ϕ) , we solve the conservation equations of mass and momentum.

In formulating the basic equations that govern the instantaneous mantle flow, the length L , velocity \mathbf{v} , stress (or pressure) $\boldsymbol{\sigma}$, are non-dimensionalized as follows:

$$L = r_1 L', \quad \mathbf{v} = \frac{\kappa_0}{r_1} \mathbf{v}', \quad \boldsymbol{\sigma} = \frac{\eta_0 \kappa_0}{r_1^2} \boldsymbol{\sigma}' \quad (\text{S5})$$

where r_1 denotes the radius of the Earth, κ_0 , the reference thermal diffusivity, and η_0 , the reference viscosity (Table S1). In these equations, symbols with primes represent non-dimensional quantities. However, for simplicity, the primes are omitted hereinafter.

Using these dimensionless factors, the dimensionless conservation equations for mass and momentum governing the instantaneous mantle flow under the Boussinesq approximation are expressed respectively as:

$$\nabla \cdot \mathbf{v} = 0 \quad (\text{S6})$$

$$-\nabla p + \nabla \cdot \left[\eta (\nabla \mathbf{v} + \nabla \mathbf{v}^{tr}) \right] + Ra_i \delta \rho \mathbf{e}_r = 0 \quad (\text{S7})$$

where \mathbf{v} is the velocity vector, p the dynamic pressure, η the viscosity, $\delta \rho$ the density anomaly, Ra_i the instantaneous Rayleigh number and \mathbf{e}_r , the unit vector in the radial direction. The superscript tr indicates the tensor transpose. The instantaneous Rayleigh number Ra_i (Yoshida, 2008) used in our computation is given by

$$Ra_i \equiv \frac{\rho_0 g b^3}{\kappa_0 \eta_0} \quad (\text{S8})$$

where ρ_0 is the reference density, g the gravitational acceleration, κ_0 the reference thermal diffusivity, η_0 the reference viscosity, and b the mantle thickness considered in the model. The physical values used in this study are listed in Table S1.

The calculation of the instantaneous mantle flow in a global 3D spherical-shell geometry has been performed using the finite-volume (FV) based mantle convection code, ConvRS (Yoshida, 2008; 2010; Adam et al., 2010; 2014). We tested different depth ranges (whole mantle convection and upper mantle convection) which will be discussed later. The number of FVs used is 132 (in r) \times 45 (in θ) \times 90 (in ϕ) for the whole mantle convection model and 32 (in r) \times 45 (in θ) \times 90 (in ϕ) for the upper mantle convection model, which means that the numerical resolution is four degrees along the horizontal directions and 22

km along the radial direction. The step along the horizontal directions has been chosen by considering that the S40RTS tomography model includes spherical harmonics up to degree and order 40, which implies a resolution of roughly 1000 km. The boundary conditions at the top and bottom of mantle are impermeable and shear-stress free.

Table S1. Physical values used in this study

Meaning of symbols	Value
Model thickness, b	660 or 2900 km
Earth's radius, r_1	6371 km
Gravitational acceleration at the surface, g	9.81 m s^{-2}
Reference density, ρ_0	3350 kg m^{-3}
Reference viscosity in the upper mantle, η_0	10^{21} Pa s
Reference thermal diffusivity, κ_0	$10^{-6} \text{ m}^2 \text{ s}^{-1}$
Instantaneous Rayleigh number, Ra_i	9.45×10^7 or 8.0×10^9
Density contrast between the mantle and sea water, $\Delta\rho_s$	2320 kg m^{-3}
Density contrast at the core-mantle boundary, $\Delta\rho_c$	4337 kg m^{-3}
Gravitational constant, G	$6.66726 \times 10^{-11} \text{ N m}^2 \text{ kg}^{-2}$

3.2 Model parameters

3.2.1 Conversion of seismic velocity anomalies into density anomalies

Deriving a quantitative geodynamical interpretation from tomography models is a difficult task. In order to obtain insightful geodynamic information from tomography models, one needs for example to convert the velocity anomalies provided by these models into temperature or density anomalies. It is an important step if one aims for example to obtain an accurate characterization of lateral viscosity variations in the mantle, or if one wants to retrieve quantitative information from the tomography models. For a realistic employment of tomography models, we integrate the results of mineral physics (Karato, 2008) in our models. These studies describe the depth dependence of the coefficient of thermal expansion, α , and of the temperature derivative of the seismic velocities anomalies for S waves as well as for P waves, $A_{VT} \equiv -\partial \ln(v)/\partial T$. In this study, we will use the α and A_{VT} given by Karato (2008) and Yoshida (2012). The depth-

dependence of the density to velocity heterogeneity ratio, $R_{\rho/v}$, on these parameters can be obtained through:

$$R_{\rho/v} \equiv \frac{\alpha}{A_{vT}} \quad (\text{S9})$$

We use the $R_{\rho/v}$ designed by Karato (2008), while assuming that the origin of the seismic velocity anomalies is purely thermal, which seems to be a fair approximation for the oceanic context, at least at the scale of resolution of the tomography model. The density anomaly can then be obtained through

$$\frac{\delta\rho}{\rho_{\text{ref}}} = R_{\rho/v} \frac{\delta v}{v_{\text{ref}}} \quad (\text{S10})$$

where δv is the seismic velocities anomaly and ρ_{ref} and v_{ref} the reference density and velocity provided in our study by the PREM model (Dziewonski and Anderson, 1981). The depth-dependency of the density to velocity heterogeneity ratio, $R_{\rho/v}$ is reported in red (full line) in Fig. S5 b). In this figure, we also show the values obtained by Lee et al. (2011), who use this coefficient as a parameter to fit the geoid anomalies. Their reference $R_{\rho/v}$ is displayed in black, and the gray lines simulate the uncertainty for this parameter. Their reference $R_{\rho/v}$ (black line) is close to 0.1 in the upper mantle, whereas the coefficient obtained from Karato (2008) parameters (red line) indicates values around 0.2. We have made several tests by varying this parameter. When we use Karato's (2008) laws, it is impossible to retrieve the observed subsidence. The amplitude of the dynamic topography is indeed twice the observed one. If we divide this parameter by a factor 2 in the upper mantle (dashed red line), the model fits well the observed depth anomalies. In the following, we will then use $R_{\rho/v}$ represented by the dashed red line in the upper mantle and the $R_{\rho/v}$ represented by the red solid line in the lower mantle. This law is comprised between the reference $R_{\rho/v}$ of Lee et al. (2011) and their left hand side uncertainty curve. In Fig. S5 a) we display the velocity anomalies along the depth cross section across the Pacific ocean represented in the inset, and in Fig. S5 c) the density anomalies computed through our model. The mantle is characterized by density anomalies of -25 kg m^{-3} in the vicinity of the EPR, and of 20 kg m^{-3} along the lithosphere of the Pacific plate. Note that we assume that the origin of the velocity anomalies is purely thermal.

3.2.2 Viscosity model

In this study, we have considered both depth and temperature dependencies of the viscosity. We consider the effect of the temperature-dependent viscosity on the mantle convection using an Arrhenius-type viscosity form

$$\eta^* = \eta(d)^* \exp\left(\frac{H_a^*}{R^*T^*} - \frac{H_a^*}{R^*T_{ref}^*}\right) \quad (S11)$$

where H_a^* is the activation enthalpy of mantle rock ($H_a^* = E_a + P.V_a$, E_a and V_a being the activation energy and volume respectively), R^* is the gas constant ($8.31 \text{ J K}^{-1} \text{ mol}^{-1}$), T^* and T_{ref}^* are the temperature and reference temperature, respectively (asterisks denote the values with dimension). Eq. (S11) is non-dimensionalized by:

$$\eta = \eta_{ref}(d) \exp\left(\frac{H_a}{T} - \frac{H_a}{T_{ref}}\right) \quad (S12)$$

where T and T_{ref} is the dimensionless temperature and reference temperature, respectively, and $\eta_{ref}(d)$ is the dimensionless reference viscosity at $T = T_{ref}$. When T_{ref} is fixed at 0.5, T can be expressed as:

$$T = T_{ref} - \gamma \delta \ln(v) = 0.5 - \gamma \delta \ln(v) \quad (S13)$$

where γ is the dimensionless coefficient defined as:

$$\gamma \equiv \frac{0.5}{A_{VT} T_{ref}^*} \quad (S14)$$

In the present study, we have considered several values of the activation energy and volume. In the upper mantle, the activation energy varies between 200 to 400 kJ/mol, and the activation volume between 2 and $4.5 \cdot 10^{-6} \text{ m}^3/\text{mol}$ (Karato and Wu, 1993; Hirth and Kohlstedt, 2003; Billen and Hirth, 2007; Lee and King, 2011). For the lower mantle, we consider the value of the activation enthalpy of MgSiO_3 perovskite in lower mantle rocks, ($H_a \sim 400 \text{ kJ mol}^{-1}$) on the basis of the result obtained from mineral physics (Yamasaki and Karato, 2001). It turns out that these parameters, although fundamentally important, do not have a major effect on the resulting viscosity and derived flow. The results displayed in the following have been obtained with $E_a = 240 \text{ kJ/mol}$, and $V_a \sim 1.5 \cdot 10^{-6} \text{ m}^3/\text{mole}$ in the upper mantle.

We impose $\eta_{\text{ref}}=1$ in the upper mantle, and therefore do not allow a depth dependency of the viscosity, because the lithosphere and asthenosphere appear clearly with respectively a high and low viscosity when considering a temperature-dependent viscosity law (see Fig. S5 d). For the lower mantle, we test several values $\eta_{\text{ref}}=1, 30, 100, 500$. The results presented hereafter have been obtained with $\eta_{\text{ref}}=100$ in the lower mantle.

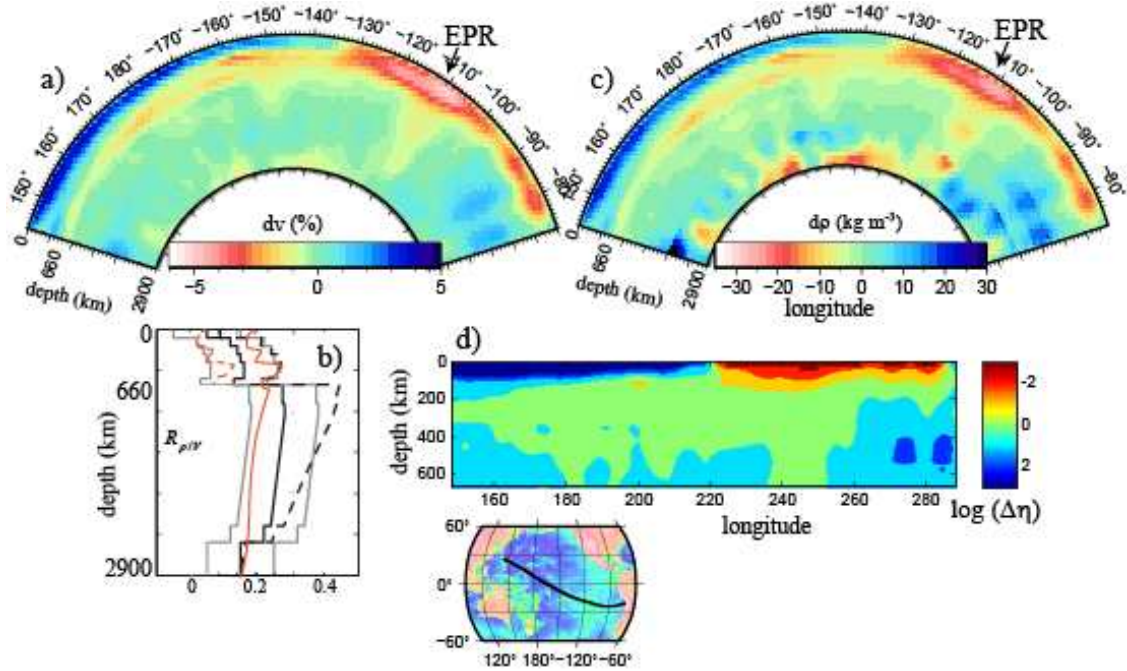


Figure S5: Mantle structure along the profile displayed in the inset. a) Seismic velocity anomalies provided by the S40RTS tomography model (Ritsema et al., 2010). b) Density to velocity heterogeneity ratio used in this study, in red, compared with other estimates from Lee et al. (2011), in grey and black. c) Density anomalies deduced from this model (see text). d) Viscosity in the upper mantle, where the lithosphere and asthenosphere appear clearly with respectively high and low viscosities.

In order to recover the lithospheric plate's motion, we also impose weak plate boundaries at the surface, by considering the plates' boundaries compilation of Bird (2003), with a viscosity of 10^{19} Pas, and introduce the regionalized upper mantle (RUM) slab model of Gudmundsson and Sambridge (1998) with a density of 50 kg m^{-3} . For the continents we impose a null density between depths 0 and 300 km, but we do not remove the shallowest part of the mantle over the oceanic areas as former studies did. Although most of the previous studies do not consider the buoyancy of the shallowest part of the mantle (Steinberger, 2007; Conrad and Husson, 2009; Spasojevic and Gurnis, 2012), some authors choose to consider it because it contains precious information about the structure and dynamics of the upper mantle and lithosphere (Forte et al., 1993; Moucha et al., 2008).

In Fig. S5 d) we display the relative viscosity along a depth cross section through the Pacific ocean. In the following, we will discuss the influence of the previously described parameters of the dynamic topography.

3.3 Sensibility of the dynamic topography to the model's parameters

The resulting dynamic topography is displayed in Fig. S6. The upper panel shows the dynamic topography considering only the upper mantle dynamics (model 1). The viscosity is temperature dependent. In the middle panel, we show the results obtained while considering the whole mantle convection (model 2). In this case, the viscosity is temperature dependent and the lower mantle is 100 times more viscous than the upper mantle. In the lowermost panel, we show the results obtained while considering the whole mantle convection induced by a model based on the S40RTS tomography model (Ritsema et al., 2011), and on the regionalized upper mantle (RUM) slab model of Gudmundsson and Sambridge (1998) with a density of 50 kg m^{-3} (model 3). In this case, the weak plate boundaries limits are imposed in the uppermost 100 km. For the continents we impose a null density between depths 0 and 300 km. In the following we will refer to this model as 'our favorite model' (model 3). In this section we will check the sensitivity of the dynamic topography, and mostly of the subsidence trend on the model's parameters.

The pattern is similar for all the considered tests, the ones considering the whole mantle convection, as well as the ones considering only the upper mantle convection. The dynamic topography presents highs over all the mid-oceanic ridges. The amplitude of the dynamic topography regularly decreases while moving away from the ridges. We also recover a positive dynamic topography south-west of the Pacific area, north of New-Zealand. Other studies, based on independent data such as the heat flow, also report an abnormally buoyant mantle over this region (Pollack et al., 1993). Over the continents, which are characterized in tomography models by faster seismic anomalies, we recover lows for the two first models. Imposing a null density anomaly over the shallowest part of the continents (model 3) changes the pattern and amplitude over the continental areas, but it does not noticeably affect the dynamic topography over the oceanic areas our study focuses on. Imposing the regionalized upper mantle (RUM) slab model also affects the dynamic topography by creating negative anomalies around the slabs, but here again it does not significantly affect on the dynamic topography over the oceanic areas.

To better illustrate the sensitivity of the subsidence trend on the model's parameters, we have reported in Fig. S7 the subsidence trend for the three previously discussed models, along a profile crossing the Pacific, displayed in the inset. The long-wavelength subsidence trend is well recovered for all the tests. As the bathymetry varies roughly between -2000 to -6000 m, and the dynamic topography is a positive quantity over the mid-oceanic ridges, we have shifted downwards the dynamic topography by 5500 to 6000 m to allow a visual comparison.

From these results it appears that the subsidence pattern is created by the upper mantle dynamics. Actually, if one imposes a lower mantle 30 to 100 times less viscous than the upper mantle, the amplitude of the long wavelength subsidence trend is almost the same than the one computed from the upper mantle only, although it changes the amplitude of intraplate features such as the South Pacific superswell (Adam et al., 2014).

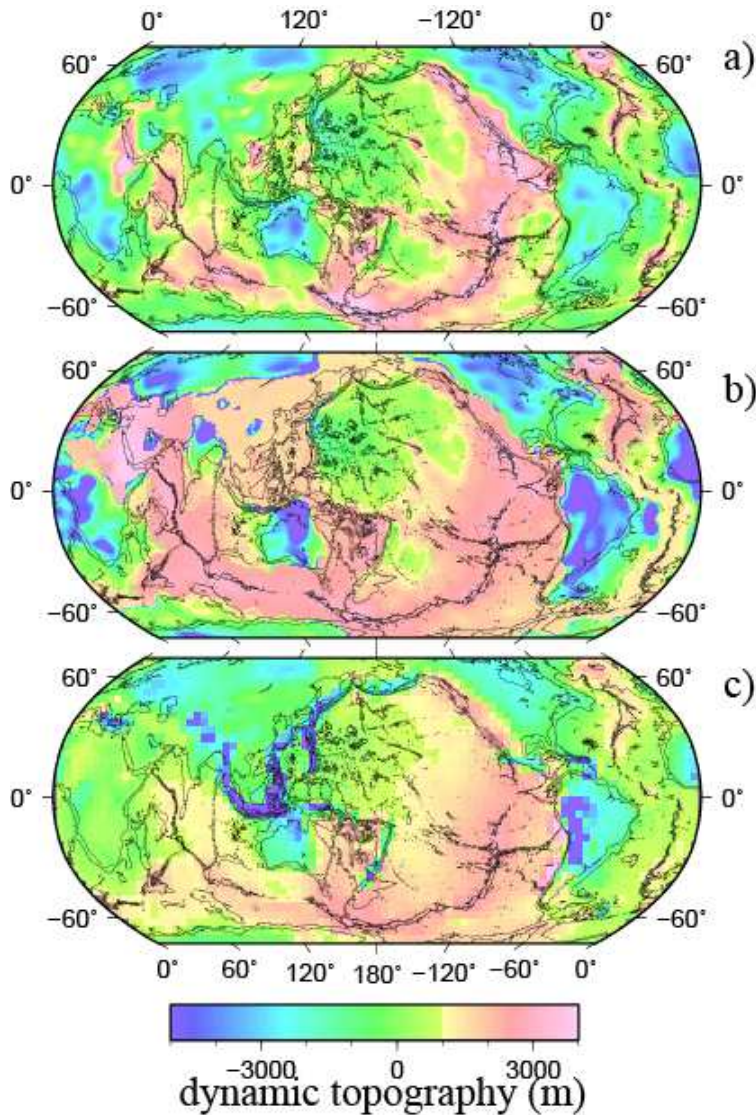


Fig. S6: Dynamic topography computed considering (a) the upper mantle dynamics only and a temperature dependent viscosity (upper panel, model 1); (b) the whole mantle dynamics and a depth and temperature dependent viscosity (middle panel, model 2); (c) the whole mantle convection induced by a model based on the S40RTS tomography model and on the regionalized upper mantle (RUM) slab model with a density of 50 kg m^{-3} (lower panel, model 3). For this last case the weak plate boundaries limits are imposed in the uppermost 100 km, and we impose a null density between depths 0 and 300 km for the continents.

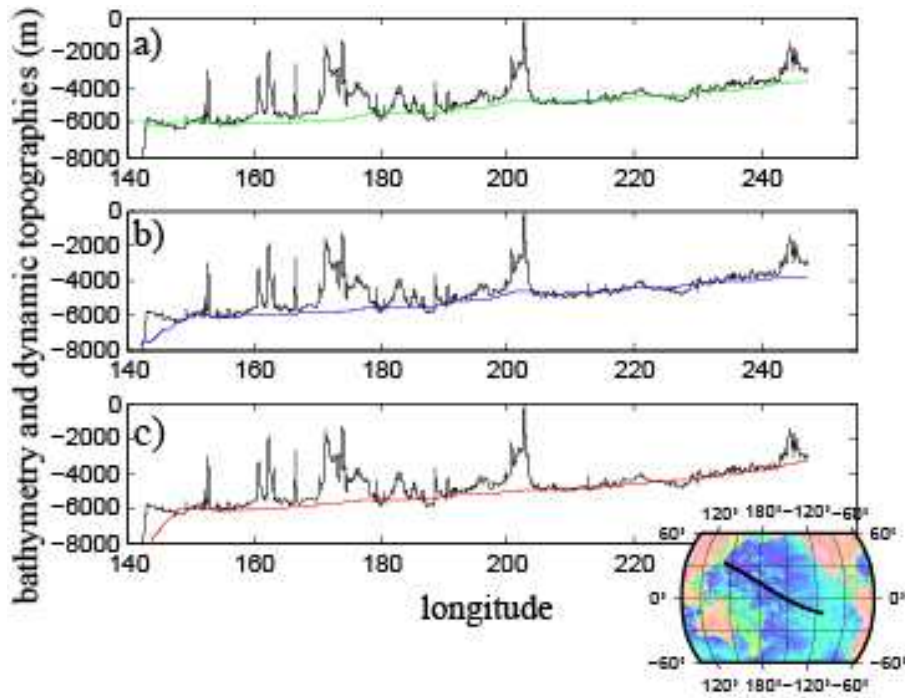
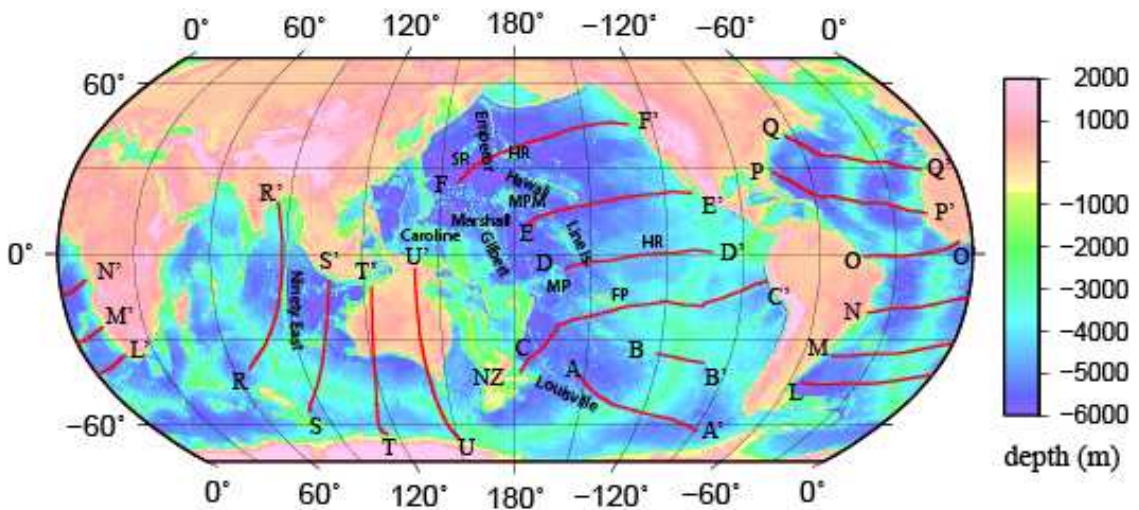
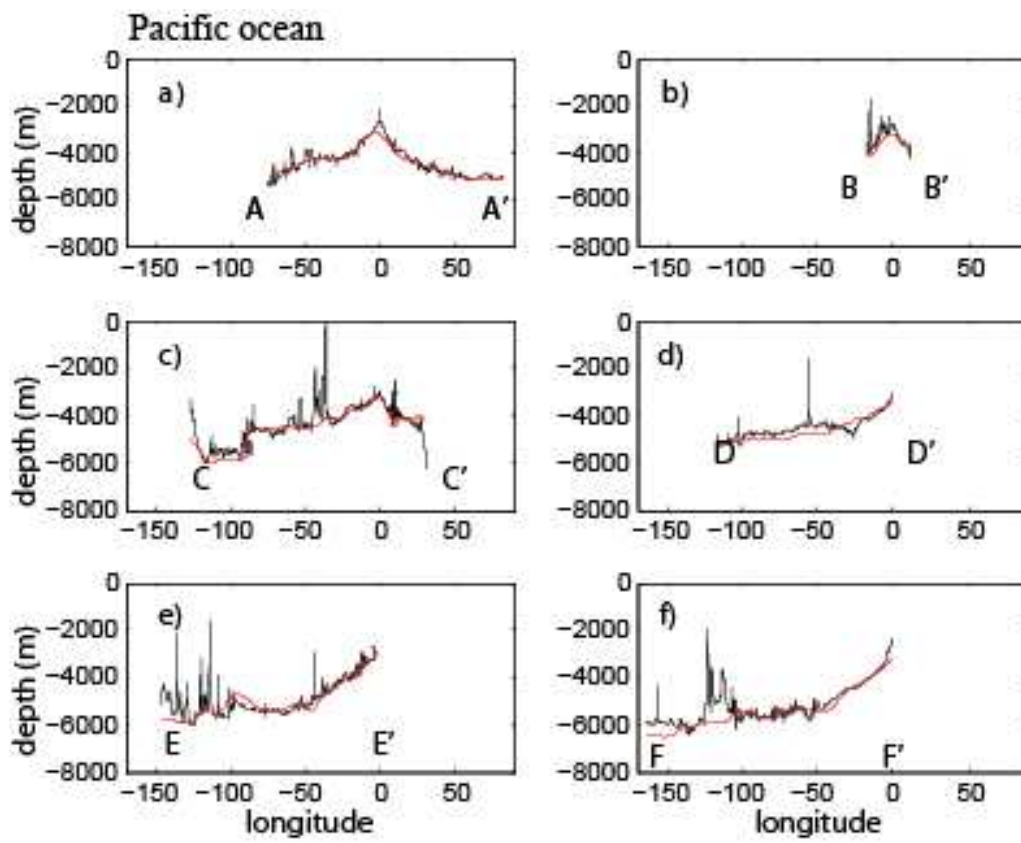


Fig. S7: Influence of the model parameters on the dynamic topography along the profile displayed in the inset. The black line is the bathymetry and the color lines the dynamic topography found through the models 1, 2, and 3 (see text and Fig. S6).

4. Dynamic topography and the subsidence trend

4.1 Qualitative correlation between the subsidence trends derived from the dynamic topography and the bathymetry





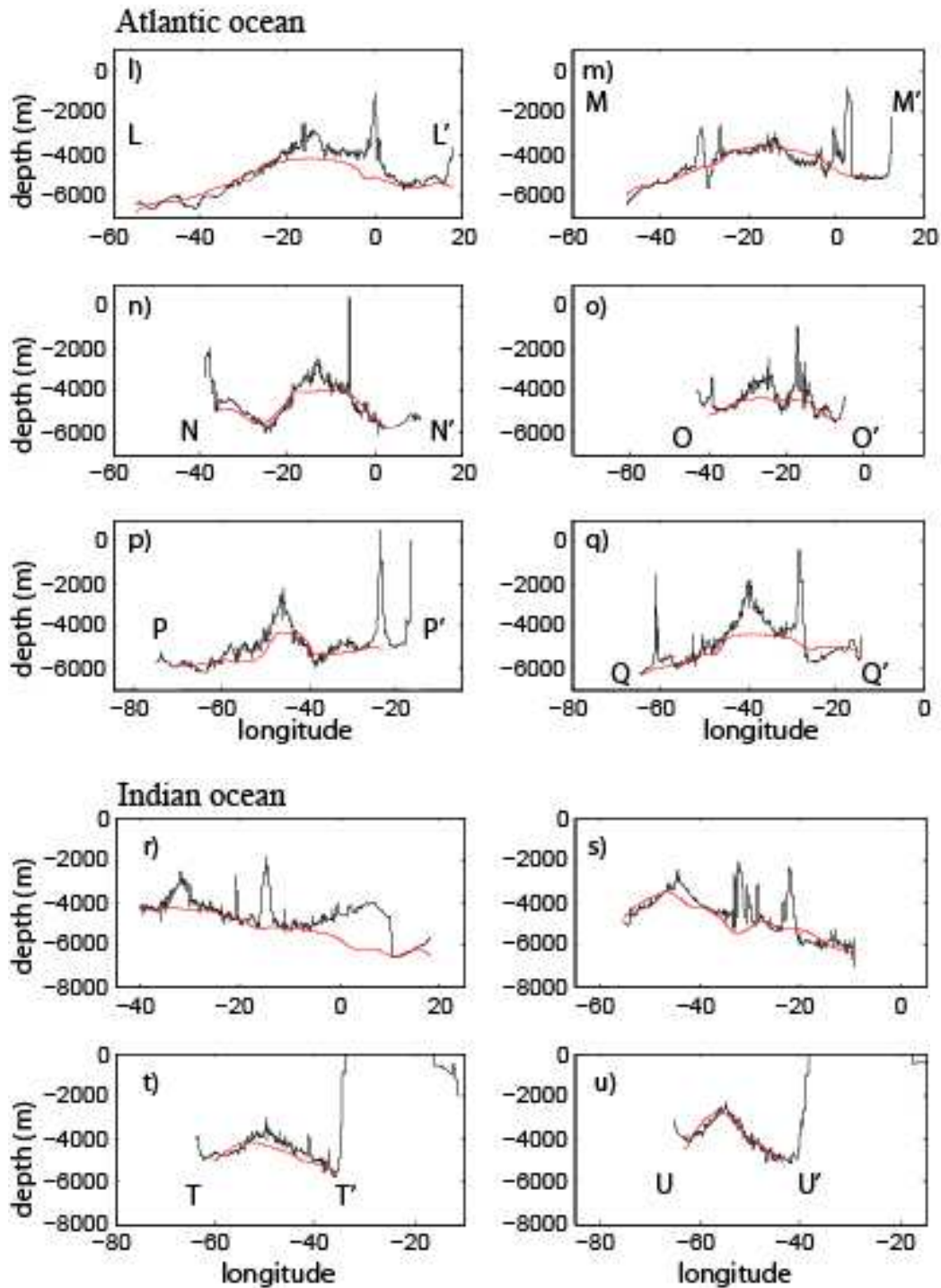


Fig. S8: Subsidence trend and dynamic topography. In the uppermost panel, we display the emplacement of the profiles along which we investigate the correlation between the bathymetry and the dynamic topography. In panels a) to u), the black lines are the bathymetry and the red lines represent the dynamic topography computed with model 3.

The comparison between the dynamic topography and the bathymetry is displayed in Fig. S8. The bathymetry varies roughly between -2000 to -8000 m, and the dynamic topography is a positive quantity, which reference value is unconstrained. Therefore, we have to adjust these two quantities in order to compare them. To allow a visual comparison, we have shifted the dynamic topography down by 5500 to 6000 m. The amplitude of the dynamic topography also varies regionally. In particular, the dynamic topography has to be multiplied by a factor two in the Indian and Atlantic oceans, in order to obtain a good correlation between the subsidence trend derived from dynamic topography and the subsidence trend observed in the bathymetry. This topic is discussed in more details in the main article.

The long wavelength of the seafloor deepening is well recovered by the dynamic topography along all the profiles. Local departures can be noted for the volcanoes, some swells, and fracture zones. We do not expect to recover the volcanoes but the swells associated with volcanic chains displaying recent activity are generally recovered by our model. Across slow and intermediate ridges such as the MAR and the SEIR, the bathymetry evolution is not well recovered. This is not surprising because intermediate and slow ridges have different characteristics than fast-spreading ridges (Ito et al., 1999; Rabinowicz et al., 2011). Indeed, it has been demonstrated that for slow mid-oceanic ridges, the mantle is characterized by faster seismic velocity anomalies although there is a layer of depleted and buoyant mantle near the surface, which controls the dynamics of these spreading centers (Rabinowicz et al., 2011).

4.2 Quantitative correlation between the subsidence trends derived from the dynamic topography and the bathymetry

In the Fig. 8 of the main paper we display the correlation between the subsidence rate deduced from the bathymetry (in black and blue) to the subsidence rate deduced from the dynamic topography (in red). Here we provide a more complete discussion on the fit of the subsidence rate derived from the dynamic topography.

For the Pacific plate (fig. 8 a), the southernmost profiles, from latitude 65°S to latitude 25°S are very short, and the ridge emplacement recovered from dynamic topography is shifted several hundreds of kilometers west from the actual ridge. We do not consider the subsidence trend derived along these profiles to be relevant. Between latitudes 25°S and 50°N, the profiles along which we derive the subsidence trend are longer. The subsidence trends computed from the bathymetry are in good agreement with the ones derived from the dynamic topography, and significantly low values are found around latitude 0°, between latitudes 20°S and 10°N. This low subsidence rate is probably created by the return flow of the South Pacific Superswell, as discussed in section 4.2 of the main paper. For the profiles between latitudes 25°S and 50°N, the emplacement of the ridge recovered from dynamic topography is sometimes shifted several hundreds of kilometers west from the actual ridge. For these profiles, the fit of the dynamic topography as the square root of the seafloor age has been done between ages 20 and 60 Ma.

For the East Pacific (Fig. 8 b), the considered profiles are too short to allow a fair estimation of the dynamic topography subsidence rates between latitudes 65°S and 37°S, and latitudes 7°S and 18°N. Longer profiles are obtained along the Nazca plate, thus allowing a more reliable computation of the dynamic topography subsidence trend. The obtained values are in good agreement with the ones deduced from the bathymetry. Around latitude 25°S, there is a sharp increase of the subsidence rate, corresponding to the location of the Easter microplate.

In the Indian ocean, there are two broad upwellings, at the westernmost extremity of the SEIR, near the location of the Balleny hotspot, and east of the SEIR, in the vicinity of St. Paul Amsterdam (see section 4.2). The upwelling near St. Paul Amsterdam is observed in the bathymetry but with a much smaller wavelength. This broad upwelling is the reason why the correlation between the subsidence rates from the dynamic topography and the bathymetry is not good between longitudes 70 and 80°E. Between longitudes 80 and 95°E, the subsidence trend observed in the bathymetry is well recovered by the dynamic topography. East of longitudes 95°E, the trajectories become very short, and it is generally harder to derive reliable subsidence trends. Moreover, the ridge in the dynamic

topography is often shifted from the bathymetric ridge (see fig. S8 r) and t)). The dynamic topography subsidence rates we report on Fig. 8 c have been obtained either by fitting the dynamic topography as the square root of the seafloor age between the '0' seafloor age and the inflexion point, or between 30 Ma (which is roughly the shift of the ridge in the dynamic topography) and the inflexion point. However, even if the fit along the westernmost trajectories is not reliable (because the trajectories are very short), we can see that the general pattern indicates a much sharper subsidence between longitudes 110 and 125°E, as already evidenced in the bathymetry.

In the west Atlantic, along the South and North American plates, the subsidence rate pattern is also roughly recovered. However, most of the time, the MAR characteristics are not very well recovered, as illustrated in fig. S8 l) to q). This is not surprising. Indeed, as stated before, former studies have demonstrated that for slow mid-oceanic ridges, the mantle is characterized by faster seismic velocity anomalies although there is a layer of depleted and buoyant mantle near the surface, that controls the dynamics of these spreading centers (Rabinowicz et al., 2011). For these reasons, most of the fits displayed in fig. 8 d) and e) have been obtained while ignoring the first 30 Ma, during which the dynamic topography displays a plateau (see Fig. S8 l) to q)). The trajectories are generally very short, especially when we ignore the first 30 Ma, and therefore the fits are not reliable. However, in the few locations where the trajectories are slightly longer, around latitude 20°N and south of 30°S, we recover a fair fit between the bathymetry and the dynamic topography subsidence rates.

In the East Atlantic, along the Nubia and Eurasia plates, the trajectories are generally too short to obtain relevant subsidence rates. The MAR issues are the same than for the West Atlantic, so the displayed fits also ignore the first 30 Ma.

As stated in the main text, the subsidence rates of the dynamic topography have been multiplied by a factor two for the Atlantic and the Indian oceans. This is discussed in more details in the main article.

References

- Adam C., V. Vidal and A. Bonneville (2005), MiFil: a method to characterize hotspot swells with application to the South Central Pacific, *Geochem. Geophys. Geosyst.*, 6, Q01003, doi:10.1029/2004GC000814
- Adam C. and A. Bonneville (2005) , Extent of the South Pacific Superswell, *J. Geophys. Res.*, 110, B09408, doi:10.1029/2004JB00346
- Adam C., M. Yoshida, T. Isse, D. Suetsugu, Y. Fukao, and G. Barruol (2010), South Pacific hotspot swells dynamically supported by mantle flows, *Geophys. Res. Lett.* 37, L08302, doi:10.1029/2010GL042534
- Adam C., M. Yoshida, D. Suetsugu, Y. Fukao, and C. Cadio (2014), Geodynamic modeling of the South Pacific Superswell, *Physics of the Earth and Planet. Int.*, 229, 24–39
- Billen, M. I., and G. Hirth (2007), Rheologic controls on slab dynamics, *Geochem. Geophys. Geosyst.*, 8, Q08012, doi:10.1029/2007GC001597.
- Bird, P. (2003), An updated digital model of plate boundaries, *Geochem. Geophys. Geosyst.*, 4(3), 1027.
- Conrad C. and L. Husson, 2009, Influence of dynamic topography on sea level and its rate of change, *LITHOSPHERE*, 1, no. 2, 110–120, doi: 10.1130/L32.1
- Dempster, A.P., N.M. Laird, D.B. Rubin (1977), Maximum-likelihood from Incomplete Data via the EM Algorithm., *J. R. Stat. Soc. B*, 39(1)
- Dziewonski, A.M. and D.L. Anderson, (1981), Preliminary reference Earth model, *Phys. Earth Planet. Inter.*, 25, 297-356.
- Forte, A.M., Peltier, W.R., Dziewonski, A.M., and Woodward, R.L., (1993), Dynamic surface topography: A new interpretation based upon mantle flow models derived from seismic tomography, *Geophys. Res. Lett.*, v. 20, no. 3, p. 225–228, doi:10.1029/93GL00249
- Fransens R., C. Strecha, L. Van Gool (2006), Robust estimation in the presence of spatially coherent outliers, *IEEE Computer Vision and Pattern Recognition Workshop*, 2006
- Gudmundsson, O., and M. Sambridge (1998), A regionalized upper mantle (RUM) seismic model, *J. Geophys. Res.*, **103**, 7121-7136.

- Hirth, G., and D. Kohlstedt (2003), Rheology of the upper mantle and the mantle wedge: A view from the experimentalists, in *Inside the Subduction Factory*, Geophys. Monogr. Ser., vol. 138, edited by J. Eiler, pp. 83–105, AGU, Washington, D. C.
- Huber, P.J. (1964), Robust Estimation of a Location Parameter, *Annals of Mathematical Statistics* 35, 1964
- Ito, G., Shen, Y., Hirth, G., and Wolfe, C.J. (1999), Mantle flow, melting, and dehydration of the Iceland mantle plume. *Earth planet. Sci. Lett.*, **165**, 81–96.
- Karato, S. I., and P. Wu (1993), Rheology of the upper mantle: A synthesis, *Science*, 260, 771–778.
- Karato, S.I. (2008), *Deformation of Earth Materials: an Introduction to the Rheology of Solid Earth*. Cambridge University Press, New York.
- Lee C.K, S. C. Hana, and B. Steinberger (2011), Influence of variable uncertainties in seismic tomography models on constraining mantle viscosity from geoid observations, *Physics of the Earth and Planet. Int.*, 184, 51–62
- Lee, C., and S.D. King (2011), Dynamic buckling of subducting slabs reconciles geological and geophysical observations, *Earth Planet. Sci. Lett.*, 312, 360–370
- Moucha, R., Forte, A.M., Mitrovica, J.X., Rowley, D.B., Quéré, S., Simmons, N.A., and Grand, S.P., (2008), Dynamic topography and long-term sea-level variations: There is no such thing as a stable continental platform, *Earth Planet. Sci. Lett.*, v. 271, no. 1–4, p. 101–108, doi:10.1016/j.epsl.2008.03.056
- Parsons, B., Sclater, J.G., (1977), An analysis of the variation of ocean floor bathymetry and heat flow with age. *J. Geophys. Res.* 82, 803–827.
- Pollack H.N., S. J. Hurter, and J. R. Johnson (1993), Heat from the Earth's Interior: Analysis of the Global data Set, *Reviews of Geophys.*, 31, 3, 267-280
- Rabinowicz, M. M. Calvet and M. J. Toplis (2011), Possible layering of mantle convection at the top of the Iceland Hotspot: a crosscheck between 3-D numerical models and gravimetric, seismic and petrological data, *Geophys. J. Int.* doi: 10.1111/j.1365-246X.2011.05250.x
- Ritsema, J., Deuss, A., van Heijst, H.J., Woodhouse, J.H. (2010), S40RTS: a degree-40 shear-velocity model for the mantle from new Rayleigh wave dispersion, teleseismic traveltime and normal-mode splitting function measurements. *J. Int. Geophys.*, 10.1111/j.1365-246X.2010.04884.x.

Rousseeuw R.J., and A.M. Leroy (1987), *Robust Regression and Outlier Detection*, Wiley

Spasojevic, S., and M. Gurnis (2012), Sea level and vertical motion of continents from dynamic Earth models since the late Cretaceous, *AAPG Bulletin*, 96(11), 2037–2064.

Stein, C., and S. Stein (1992), A model for the global variation in oceanic depth and heat flow with lithospheric age, *Nature*, **359**, 123-129.

Steinberger, B., (2007), Effects of latent heat release at phase boundaries on flow in the Earth's mantle, phase boundary topography and dynamic topography at the Earth's surface, *Physics of the Earth and Planet. Int.*, v. 164, no. 1–2, p. 2–20, doi:10.1016/j.pepi.2007.04.021

Takeuchi I., Y. Bengio, T. Kanamori (2002), Robust regression with asymmetric heavy-tail noise distributions, *Neural computation* 14(10), 2002

Yamazaki, D., Karato, S. (2001), Some mineral physics constraints on the rheology and geothermal structure of Earth's lower mantle. *Am. Mineral.* 86, 385–391.

Yoshida, M. (2008), Core-mantle boundary topography estimated from numerical simulations of instantaneous mantle flow, *Geochem. Geophys. Geosyst.*, 9, Q07002, doi:10.1029/2008GC002008.

Yoshida, M. (2010), Preliminary three-dimensional model of mantle convection with deformable, mobile continental lithosphere, *Earth Planet. Sci. Lett.*, 295(1-2), 205-218, doi:10.1016/j.epsl.2010.04.001.

Yoshida, M., Tajima, F., Honda, S., Morishige, M. (2012), The 3D numerical modeling of subduction dynamics: plate stagnation and segmentation, and crustal advection in the wet mantle transition zone. *J. Geophys. Res.* 117 (B4), B04104. <http://dx.doi.org/10.1029/2011JB008989>.

Weisstein. E.W, Least Squares Fitting. From MathWorld--A Wolfram Web Resource. <http://mathworld.wolfram.com/LeastSquaresFitting.html>